

Tertiary and Quaternary States in the Taylor-Couette System

T. Akinaga

Department of Mechanical Engineering, Graduate School of Engineering & Resource Science, Akita University, Akita 010-8502, Japan

S. C. Generalis*

Mathematics, School of Engineering and Applied Sciences, Aston University, Birmingham B4 7ET, United Kingdom

F. H. Busse

Institute of Physics, University of Bayreuth, Bayreuth D-95440, Germany

Abstract

The analysis of the Taylor-Couette problem in the small gap limit is extended to the cases of tertiary and quaternary solutions. The theoretical results are compared with experimental observations. Although in the latter the small-gap approximation is not always well approximated, the comparison of theoretical results and observations yields reasonable agreements. The absence of the wavy twist mode in the observed patterns is explained by the presence of no-slip boundary conditions in the axial direction of the experimental apparatus, which differ from the periodic conditions imposed in the theoretical analysis. Quaternary solutions bifurcating from the tertiary ones through subharmonic instabilities are presented and compared with experimental observations. Reasonable agreement has been found.

Keywords: Bifurcation theory, nonlinearity, Floquet parameters, stability

1. Introduction

The Taylor-Couette system continues to fascinate experimental as well as theoretical fluid dynamicists by its rich variety of flow patterns. This variety is best illustrated by the famous Figure 1 of the paper by [1], in which the numerous observed patterns have been indicated as functions of the rotation rates of two independently rotating co-axial cylinders. Since that time several new experimental and theoretical studies have been prepared and this research is likely to continue in the future since a complete understanding of the various patterns of fluid flow in the Taylor-Couette system can still not be claimed. For a recent assessment of the role of the Taylor-Couette problem in the general field of fluid dynamics we refer to [2] and for an earlier review to [3].

In the present paper extensions of the analysis of [4] (to which we shall refer to in the following by WBN) will be presented. Our investigations are motivated by the experimental work of [5] (to which we shall refer to in the following by HBA) and by the more recent plane-Couette flow experiments carried out on a turntable by [6] (referred to hereafter by TTA) and by [7] (referred to by SSA).

In the paper WBN the small-gap approximation was employed for the theoretical analysis of the Taylor-Couette problem. In the small gap limit a symmetry is gained and the number of parameters is reduced by one. The fact that the more recent experimental observations of HBA have confirmed the stability boundaries for the onset of twist vortices even though the radius ratio of their cylindrical boundaries, $r_i/r_o = 0.88$, differed considerably from the small gap limit, $r_i/r_o \approx 1$, encourages us to continue the use of the small gap approximation. The small gap approximation or equivalently the plane Couette flow problem in a system rotating about an axis in the span-wise direction has also been employed by [8] and recently by [9]. [8] has focussed the attention on low rotation rates and referred to [10] for comparisons with experimental observations. Similarly [9] emphasized low rotation rates with the goal of comparisons with the experimental results of TTA and SSA. Because these experiments employed a Couette apparatus on a turn-table the observations had to be restricted to relative small values of the rotation rate. In the present work larger values of the rotation rate will be considered and comparisons will be made with observations of HBA based on a cylindrical apparatus.

A comparison with the observations of HBA has also been performed by [11] (to which we shall refer in the following by AnS) who performed numerical computations of patterns of the Taylor-Couette system for different radius ratios of the cylindrical boundaries. Among those ratios they included the case $r_i/r_o = 0.88$ used by HBA. Wherever a comparison with the results of WBN has been possible AnS found good agreement. We regard this as additional support for our use of the small gap approximation. On the other hand the use of the experimental aspect ratio is not sufficient for a

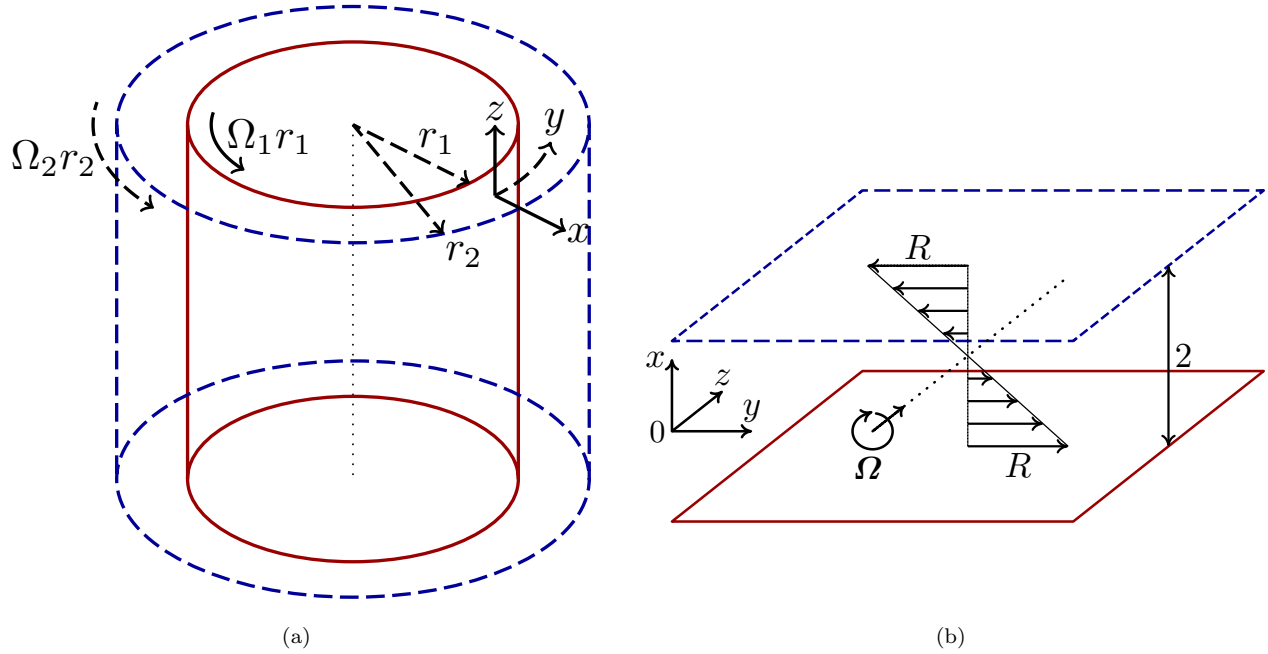


Figure 1: Taylor-Couette systems. (a) Circular Taylor-Couette system: two co-axial cylinders of radii r_1 and r_2 , rotating with different speeds $\Omega_1 r_1$ and $\Omega_2 r_2$, respectively. (b) Narrow gap limit of the circular Taylor-Couette system (rotating plane Couette flow): the system is rotating with angular velocity $\mathbf{\Omega} = (0, 0, \Omega/2)$ and the two plates are drifting with a relative velocity $(0, 2R, 0)$. The dimensional gap width between the two infinite plates is $2h$. The x , y and z coordinates in the narrow gap planar system (b) correspond to the radial, azimuthal and axial directions in the circular Taylor-Couette system (a), respectively. Note that (b) refers to the dimensionless system.

29 perfect agreement between theory and observation since the usual employment of periodic boundary conditions in the
 30 axial direction causes deviations from the experimental conditions.

31 The basic equations are formulated and discussed in section 2. There we also describe the numerical methods applied
 32 for their solutions. In section 3 the basic properties of the small gap Taylor-Couette system will be surveyed in terms of
 33 Taylor vortices with the critical wavelength and their subsequent bifurcations. As has been demonstrated by HBA the
 34 properties of solutions bifurcating from axisymmetric Taylor vortices and from tertiary solutions depend rather strongly
 35 on the basic wavelength of the vortices. Hence in section 4 we outline stability boundaries for four of the different basic
 36 wavelengths investigated by HBA. Our conclusions are given in section 5.

37 2. Mathematical formulation of the problem

38 We consider the flow in the narrow gap between two co-axial cylinders with radii r_1 and r_2 that are rotating with
 39 speeds $\Omega_1 r_1$ and $\Omega_2 r_2$, respectively. Half of the gap width, $h \equiv (r_2 - r_1)/2$ will be used as length scale in the following
 40 and h^2/ν is used as timescale, where ν is the kinematic viscosity of the fluid. We assume the limit h/r_1 tending to zero
 41 and introduce a Cartesian system of coordinates with x , y , z in the radial, azimuthal and axial directions, respectively,
 42 as shown in Figure 1. The corresponding unit vectors are denoted by \mathbf{i} , \mathbf{j} , \mathbf{k} . The dimensionless Navier-Stokes equations
 43 can then be obtained in the form:

$$\left[\frac{\partial}{\partial t} + \mathbf{u} \cdot \nabla \right] \mathbf{u} + \Omega \mathbf{k} \times \mathbf{u} = -\nabla \pi + \nabla^2 \mathbf{u}, \quad (1)$$

$$\nabla \cdot \mathbf{u} = 0, \quad (2)$$

where Ω is twice the mean rotation rate in dimensionless units,

$$\Omega = (\Omega_1 + \Omega_2) h^2 / \nu. \quad (3)$$

The boundary conditions are given by

$$\mathbf{u} = \mp R \mathbf{j} \quad \text{at} \quad x = \pm 1, \quad (4)$$

where the Reynolds number R is defined by

$$R \equiv h (\Omega_1 - \Omega_2) (r_1 + r_2) / (4\nu). \quad (5)$$

It is convenient to eliminate the equation of continuity (2) by the introduction of the following general representation of the velocity field :

$$\begin{aligned}\mathbf{u} &= [-Rx + V(t, x)]\mathbf{j} + W(t, x)\mathbf{k} + \tilde{\mathbf{u}}, \\ \tilde{\mathbf{u}} &= \nabla \times [\nabla \times \mathbf{i}\phi(t, \mathbf{x})] + \nabla \times \mathbf{i}\psi(t, \mathbf{x}).\end{aligned}\quad (6)$$

Accordingly $\tilde{\mathbf{u}}$ can be expressed in the form

$$\tilde{\mathbf{u}} = -\Delta_2\phi\mathbf{i} + \left[\frac{\partial^2\phi}{\partial x\partial y} + \frac{\partial\psi}{\partial z}\right]\mathbf{j} + \left[\frac{\partial^2\phi}{\partial z\partial x} - \frac{\partial\psi}{\partial y}\right]\mathbf{k},\quad (7)$$

where the operator Δ_2 is defined by $\Delta_2 \equiv \nabla^2 - (\mathbf{i} \cdot \nabla)^2$. By operating with $\mathbf{i} \cdot \nabla \times (\nabla \times \circ)$ and $\mathbf{i} \cdot \nabla \times \circ$ on equation (1) we obtain the following two equations for $\phi(t, \mathbf{x})$ and $\psi(t, \mathbf{x})$:

$$\begin{aligned}\left[\nabla^2 - \frac{\partial}{\partial t}\right]\nabla^2\Delta_2\phi - \Omega\frac{\partial}{\partial z}\Delta_2\psi &= (-Rx + V)\frac{\partial}{\partial y}\nabla^2\Delta_2\phi - \frac{\partial^2 V}{\partial x^2}\frac{\partial}{\partial y}\Delta_2\phi \\ &\quad - \frac{\partial^2 W}{\partial x^2}\frac{\partial}{\partial z}\Delta_2\phi + W\frac{\partial}{\partial z}\nabla^2\Delta_2\phi + \mathbf{i} \cdot \nabla \times [\nabla \times (\tilde{\mathbf{u}} \cdot \nabla \tilde{\mathbf{u}})],\end{aligned}\quad (8)$$

$$\begin{aligned}\left[\nabla^2 - \frac{\partial}{\partial t}\right]\Delta_2\psi + \Omega\frac{\partial}{\partial z}\Delta_2\phi &= (-Rx + V)\frac{\partial}{\partial y}\Delta_2\psi + \left[R - \frac{\partial V}{\partial x}\right]\frac{\partial}{\partial z}\Delta_2\phi \\ &\quad + W\frac{\partial}{\partial z}\Delta_2\psi + \frac{\partial W}{\partial x}\frac{\partial}{\partial y}\Delta_2\phi - \mathbf{i} \cdot \nabla \times (\tilde{\mathbf{u}} \cdot \nabla \tilde{\mathbf{u}}).\end{aligned}\quad (9)$$

The mean flows in the azimuthal and axial directions obey the equations

$$\left[\frac{\partial^2}{\partial x^2} - \frac{\partial}{\partial t}\right]V = -\frac{\partial}{\partial x}\overline{\Delta_2\phi\left[\frac{\partial^2}{\partial x\partial y}\phi + \frac{\partial}{\partial z}\psi\right]},\quad (10)$$

$$\left[\frac{\partial^2}{\partial x^2} - \frac{\partial}{\partial t}\right]W = -\frac{\partial}{\partial x}\overline{\Delta_2\phi\left[\frac{\partial^2}{\partial z\partial x}\phi - \frac{\partial}{\partial y}\psi\right]},\quad (11)$$

44 where the bar indicates the average over surfaces $x = \text{constant}$.

Note that the mean flow W in the axial direction was not considered in WBN, in contrast to the present study, where we allow mean flows in both directions. The requirement of vanishing velocity at the boundaries implies the conditions:

$$\phi = \frac{\partial\phi}{\partial x} = \psi = V = W = 0 \quad \text{at} \quad x = \pm 1.\quad (12)$$

45 2.1. Harmonic expansion and stability analysis

We assume periodicity in both stream-wise (y) and span-wise (z) directions, whereas non-slip boundary conditions are imposed at $x = \pm 1$. For the poloidal (ϕ) and toroidal (ψ) components in equation (6), we assume the following expansions:

$$\begin{aligned}\phi &= \sum_{\ell=0}^L \sum_{\substack{|m|\leq M, |n|\leq N \\ (m,n)\neq(0,0)}} \phi_{\ell mn} F_{\ell}(x) \exp[im\alpha(y - ct) + in\beta z], \\ \psi &= \sum_{\ell=0}^L \sum_{\substack{|m|\leq M, |n|\leq N \\ (m,n)\neq(0,0)}} \psi_{\ell mn} G_{\ell}(x) \exp[im\alpha(y - ct) + in\beta z].\end{aligned}\quad (13)$$

In expressions (13) we have incorporated the phase speed c in order to account for steady ($\phi(\mathbf{x}), \psi(\mathbf{x}), c = 0$) as well as shape preserving traveling wave solutions with the uniform velocity field ($\phi(\mathbf{x}), \psi(\mathbf{x}), c \neq 0$). $F_{\ell}(x)$ and $G_{\ell}(x)$ ($\ell = 0, 1, \dots, L$) are combinations of the 1st kind Chebyshev polynomials ($T_{\ell}(x)$ ($\ell = 0, 1, \dots$)),

$$F_{\ell}(x) = \frac{(\ell + 1)T_{\ell+4}(x) - 2(\ell + 2)T_{\ell+2}(x) + (\ell + 3)T_{\ell}(x)}{4(\ell + 2)},\quad (14)$$

$$G_{\ell}(x) = \frac{T_{\ell}(x) - T_{\ell+2}(x)}{2},\quad (15)$$

that are employed in order to satisfy

$$F_{\ell} = \frac{dF_{\ell}}{dx} = G_{\ell} = 0 \quad \text{at} \quad x = \pm 1.\quad (16)$$

For the mean flows in the azimuthal and axial directions we write:

$$V(x) = \sum_{\ell=0}^L V_{\ell} G_{\ell}(x), \quad (17)$$

$$W(x) = \sum_{\ell=0}^L W_{\ell} G_{\ell}(x) + \mu (x^2 - 1), \quad (18)$$

where μ is determined by the condition of vanishing mass flux in the z -direction,

$$\int_{-1}^{+1} W(x) dx = 0. \quad (19)$$

46 This ensures that our numerical model represents the properties of the usual experimental set-ups. The integer values
 47 L, M, N represent the truncation parameters and $\phi_{\ell mn}, \psi_{\ell mn}, V_{\ell}, W_{\ell}$ are coefficients to be determined. The values $L, M,$
 48 N must be sufficiently high such that the numerical solutions do not change significantly if L, M, N are increased. For
 49 example the level $(L, M, N) = (17, 8, 17)$ is selected for the Twisolution and for $R \leq 150$, which yields a relative error of
 50 less than 1%. For states arising from a subharmonic instability as much as twice the truncation level mentioned above
 51 must be employed in the respective directions. This inevitably results in a large number of coefficients $\phi_{\ell mn}, \psi_{\ell mn}, V_{\ell}$
 52 and W_{ℓ} from eqs. (8-11), that need to be determined. Additionally, symmetries of the nonlinear states have been used in
 53 order to reduce the number of independent coefficients.

54 In order to analyse the stability of steady or steadily drifting solutions we use Floquet analysis and we superimpose
 55 complex infinitesimal disturbances $\tilde{\phi}, \tilde{\psi}$ onto ϕ and ψ , respectively,

$$\begin{aligned} \tilde{\phi} &= \sum_{\ell=0}^L \sum_{\substack{|m| \leq M, |n| \leq N \\ (m,n) \neq (0,0)}} \tilde{\phi}_{\ell mn} F_{\ell}(x) \exp [i(m\alpha + d)(y - ct) + i(n\beta + b)z + \sigma t], \\ \tilde{\psi} &= \sum_{\ell=0}^L \sum_{\substack{|m| \leq M, |n| \leq N \\ (m,n) \neq (0,0)}} \tilde{\psi}_{\ell mn} G_{\ell}(x) \exp [i(m\alpha + d)(y - ct) + i(n\beta + b)z + \sigma t]. \end{aligned} \quad (20)$$

The disturbances satisfy the boundary conditions:

$$\tilde{\phi} = \frac{\partial \tilde{\phi}}{\partial x} = \tilde{\psi} = 0 \quad \text{at} \quad x = \pm 1. \quad (21)$$

56 Herein the value of $d^2 + b^2$ is assumed to be different from zero in the stability analysis, and therefore no contributions
 57 to the mean flows in the azimuthal and axial directions are taken into account. If the real part σ_r of the growth rate σ is
 58 positive anywhere as a function of the Floquet parameters d and b , then the steady solution is unstable; otherwise it is
 59 regarded as stable.
 60

61 Direct Numerical Simulations (DNS) are employed mainly for the cases where time dependent solutions need to be
 62 determined, that do not lead to shape preserving traveling waves. The evolution in time of the oscillatory states is
 63 analysed through integration in time of the system of equations for the expansion coefficients $\phi_{\ell mn}(t)$ and $\psi_{\ell mn}(t)$ in the
 64 general representation (13). The truncation level is determined in the same way as in the case of steady state solutions
 65 or shape preserving traveling waves. In order to determine the stability range of these oscillatory states we introduce
 66 perturbations on the leading coefficients and observe their evolution in time. The oscillatory state is considered stable for
 67 the range of Reynolds numbers and rotation rates, for which a converged solution (that remains unchanged with further
 68 time integrations) can be identified.

69 3. Taylor vortices with the critical wavelength and their instabilities

It is well known from previous work (see for example [12]) that the onset of instability in the form of Taylor vortices
 of the y, z -independent basic state occurs for

$$R = \frac{106.8}{\Omega} + \Omega$$

70 in the small gap limit with nearly co-rotating cylinders, to which we restrict attention in this paper. The y -independent
 71 solution bifurcating from the state $V_0 = -Rx$ is characterised by the critical value $\beta_c = 1.558$ of the wavenumber β and
 72 is called Taylor vortex flow (Tv). As this solution evolves as a function of the parameters R and Ω it encounters stability
 73 boundaries corresponding to the onset of three-dimensional disturbances of the various kinds as indicated in Figure 2. The

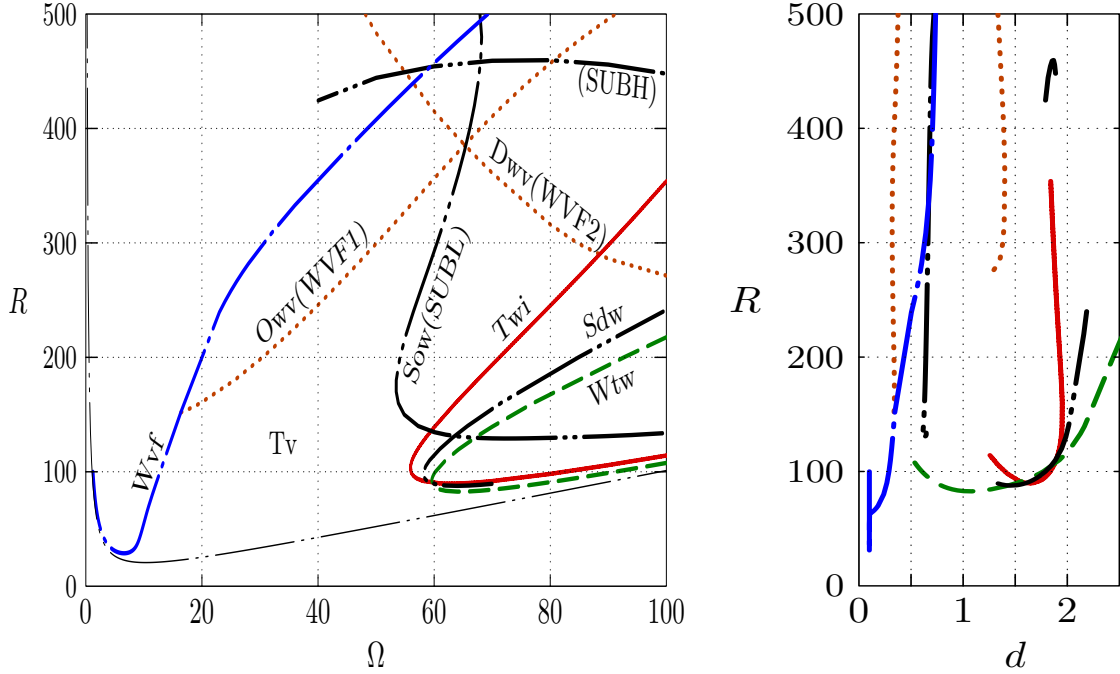


Figure 2: Stability boundaries of Taylor vortices (Tv) for $\beta = \beta_c = 1.558$ in the narrow gap limit. The results of the present analysis with $(L, M, N) = (25, 0, 25)$ can be compared with those of NAG (corresponding to the terms in brackets), where the monotonic and oscillatory instabilities of Tv for the critical value of β have first been presented. The right plot displays the value of the parameter d (here $b = 0$, see equations (20)), for which the real part σ_r of the growth rate σ becomes positive, thus determining the boundaries on the left plot. The types of curves between the two plots are in one to one correspondence. The outer (thin) curve is the neutral stability boundary.

Orders	States	Short names	HBA	NAG
Secondary	Taylor vortex flow	Tv	TVF	TVF
Tertiary	Ordinary twists (Twist vortices)	Twi	TWI	TTF
	Wavy twists	Wtw	–	–
	Wavy vortex flow	Wvf	WVF	WVF
	Oscillatory wavy vortex flow	Owv	WVF	WVF1
	Drifting wavy vortex flow	Dwv	–	WVF2
	Subharmonic oscillatory wavy vortex	Sow	WOB	SUBL
	Subharmonic drifting wavy vortex	Sdw	–	–
	Quaternary	Subharmonic wavy inflow boundary	Swib	TWI+WIB
	Subharmonic wavy outflow boundary	Swob	–	–
	Subharmonic oscillatory wavy vortex flow	Sowv	–	–

Table 1: Nomenclature for states of flow used by HBA, NAG, WBN and the present study. We note that the Wavy inflow/outflow boundary states were reported as tertiary states in NAG, and that there are other wavy inflow boundary states (not denoted as TWI+WIB) in HBA.

L, N	$R = 140$	240	340	440
13	(0.04945, ± 34.218)	(0.27110, ± 48.428)	(0.05073, ± 61.550)	(0.01866, ± 74.919)
17	(0.08403, ± 34.225)	(0.21255, ± 48.379)	(-0.75724, ± 62.042)	(-2.03224, ± 77.715)
21	(0.08577, ± 34.226)	(0.19636, ± 48.393)	(-0.79080, ± 62.230)	(-1.93737, ± 78.023)
25	(0.08579, ± 34.226)	(0.19449, ± 48.395)	(-0.79093, ± 62.233)	(-1.95085, ± 78.004)
29	(0.08580, ± 34.226)	(0.19448, ± 48.395)	(-0.79058, ± 62.233)	(-1.95038, ± 78.005)

Table 2: Numerical accuracy: convergence of the real (σ_r) and imaginary (σ_i) parts of the leading eigenvalue $\sigma = (\sigma_r, \sigma_i)$, as a function of the truncation level, close to the stability boundary of Sow for $\beta = 1.558$. $b = 0.779$. $(\Omega, d) = (58, 0.619)$, $(57, 0.651)$, $(61, 0.682)$ and $(62, 0.748)$ are for $R = 140, 240, 340$ and 440 , respectively.

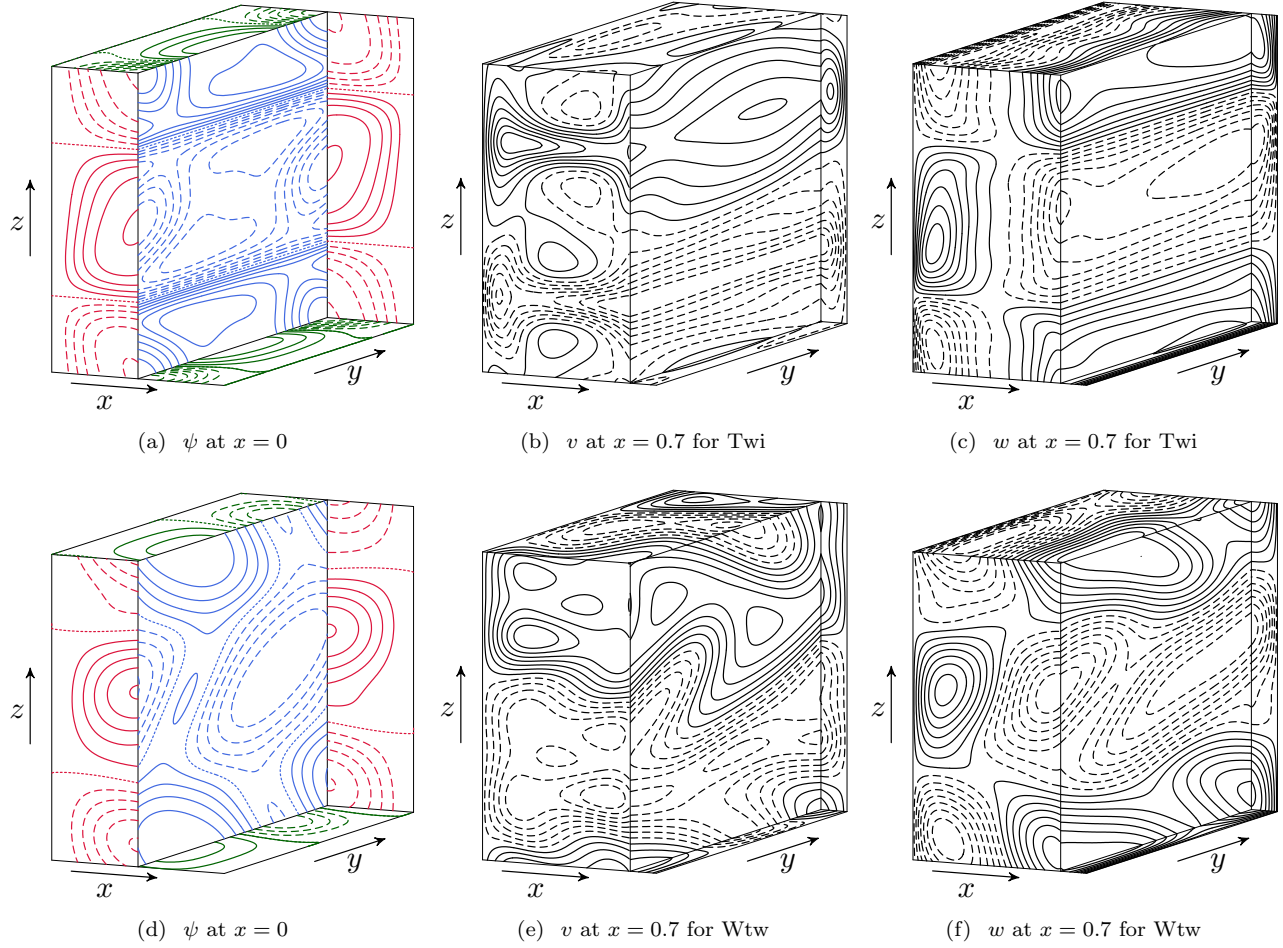


Figure 3: Tertiary states for $\beta = 1.25$ visualised by the potential ψ : (a) ordinary twists (Twi) for $(R, \Omega, \alpha) = (150, 50, 1.7)$ and (d) wavy twists (Wtw) for $(75, 65, 0.6)$. ψ is plotted on the plane $x = 0$, whereas (b)-(c) and (e)-(f) are contour plots at $x = 0.7$ for the azimuthal, $v = \frac{\partial^2 \phi}{\partial x \partial y} + \frac{\partial \psi}{\partial z}$, and axial, $w = \frac{\partial^2 \phi}{\partial x \partial z} - \frac{\partial \psi}{\partial y}$, components of the velocity field for the tertiary states Twi and Wtw as indicated.

74 nomenclature for states of flow used by HBA, NAG, WBN and the present study is listed in Table 1, while the convergence
75 of eigenvalues with respect to truncation levels is shown in Table 2 for the tertiary state Sow as an example.

76 In the left plot of Figure 2 we have indicated the stability boundaries resulting from our stability analysis. The names
77 in brackets on the curves are based on Figure 2 of [13] (hereafter referred to as NAG). In the plot on the right hand side
78 the values of the parameter d (which defines the value of the azimuthal wavenumber α for the tertiary state)
79 for which the maximum growth rate vanishes. In distinction from NAG in the present study Dwv (WVF2), corresponding
80 to a maximum growth rate for $d \sim 1.4$ is placed below the SUBH (corresponding to a maximum growth rate for $d \sim 1.8$).
81 This latter stability boundary thus does not have any physical meaning since it is preceded by the Dwv-instability.

82 The finite-amplitude tertiary solutions corresponding to Wtw and Twi were described in WBN, and they are confirmed
83 in this work to bifurcate always supercritically. A useful measure of characterization of finite-amplitude solutions is given
84 by the azimuthal component of the torque, $\tau_{\pm} = R - \frac{dV}{dx} |_{\pm 1}$, which is exerted on the cylinders.

85 Table 1 of WBN compares $\tau = \tau_{\pm}$ of Twi and Wtw with values of τ of the (unstable) two-dimensional solutions at
86 the same points in the parameter space. It is shown in WBN that the torques of the tertiary flows always increase with
87 Reynolds number, but are smaller than the torque values of the corresponding Taylor vortex solution. Twi were found to
88 be stable at intermediate rotation number values, while Wtw were found to be stable at higher Ω . WBN also noted that
89 there is a regime around $\Omega/R = 0.7$, where no stable states could be obtained.

90 In order to show a detailed comparison between our numerical scheme and that of WBN we present Table 3. Here
91 examples from WBN for the torque τ of the secondary Tv and of the tertiary Twi and Wtw solutions, are compared
92 directly with our own results. The truncation levels used in WBN and in the present work differ, but the agreement
93 between the two studies is very good. We note that the truncation level that was employed throughout the present work
94 exceeds the minimum truncation level, for which a good agreement is achieved for the tertiary twist solutions of the present
95 and the WBN studies.

	Torque τ						Ω/R	α
	R_{II}	R	2D	3D	3D			
Twi	99.41	103.02	241.19 239.67	239.67 ($N_T = 10$) 238.67 (17, 5, 17)	239.53 ($N_T = 9$) 238.68 (15, 3, 15)		0.55	1.81
Wtw	81.88	87.02	125.32 125.20	124.69 ($N_T = 10$) 124.59 (17, 5, 17)	124.68 ($N_T = 9$) 124.53 (13, 3, 13)		0.80	0.99

Table 3: Torque τ per unit area of a Taylor vortex and for twisted solutions with $\beta = 1.55$. R_{II} is the corresponding critical value of R for the onset of the tertiary solutions. R_{II} and R are the values of R quoted in Table 1 of WBN. The results for the secondary and tertiary states of WBN are quoted above those of the present work. N_T and (L, M, N) refer to the truncation levels of WBN and of the present work, respectively. In WBN $\ell + |m| + |n| \leq N_T = 10$ and $|m| \leq m_T = 4$ were used.

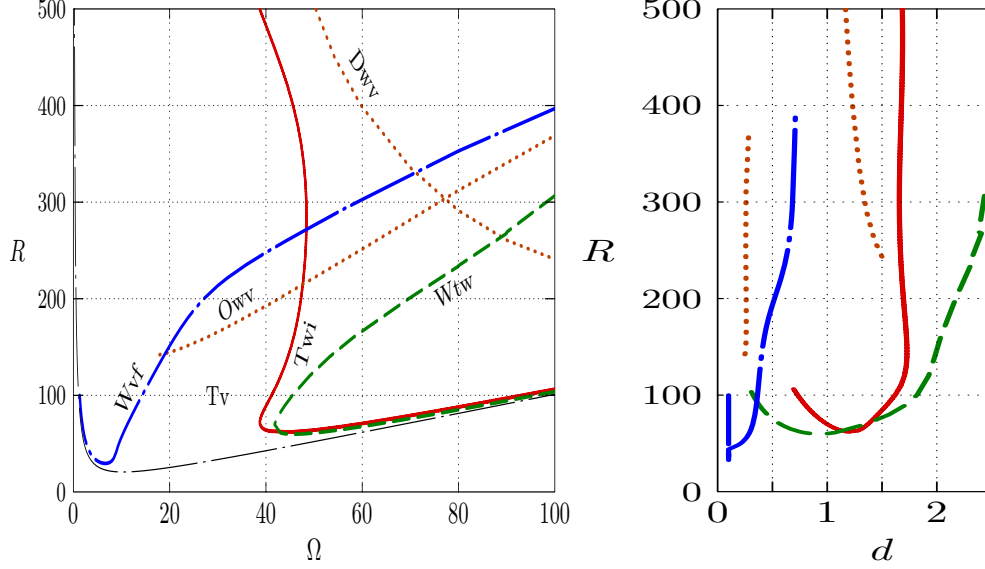


Figure 4: Stability boundaries of Tv for $\beta = 1.257$. Here $(L, M, N) = (25, 0, 25)$. These boundaries correspond to the onset of the ordinary twists (Twi, thick solid line), of wavy twists (Wtw, dashed line), of wavy vortex states (Wvf, dash-dotted line) and of the oscillatory wavy vortex states (Owv, dotted line). The right plot displays the value of the parameter d (see eqs.(20)), for which the real part σ_r of the growth rate σ becomes positive, thus determining the boundaries on the left plot.

According to WBN we can write for $\tilde{\mathbf{u}}$ of (6):

$$\tilde{\mathbf{u}} = \tilde{u}\mathbf{i} + \tilde{v}\mathbf{j} + \tilde{w}\mathbf{k} = \nabla \times \mathbf{i}\psi + \nabla \times \mathbf{j}\phi_1 + \nabla \times \mathbf{k}\phi_2, \quad (22)$$

where

$$\phi_1 = \frac{\partial \phi}{\partial z}, \quad \phi_2 = -\frac{\partial \phi}{\partial y}. \quad (23)$$

Formulae (22, 23) thus allow a three-dimensional graphic representation of the velocity field through contour plots of the potentials ψ , ϕ_1 , ϕ_2 in the planes perpendicular to \mathbf{i} , \mathbf{j} , \mathbf{k} . We show typical examples of the Twi and Wtw states, using the WBN representation of the disturbances, in Figure 3. As noted in WBN (see also Figure 3) the axial wavelength for Twi is larger by a factor of 1.3 than the azimuthal wavelength, while for Wtw the azimuthal wavelength is significantly longer than the axial wavelength. The stability boundaries of the tertiary twist solutions are discussed in the following section.

4. Comparisons with Experimental Observations

4.1. Tertiary states

In experimental studies of the Taylor-Couette system a broad range of vortex patterns has been realised. Besides vortices with the critical wavenumber β_c broader vortices corresponding to smaller values of β have been generated. In order to make a direct comparison of our narrow gap approach and the work of HBA we selected a set of four values of the axial wavenumber: $\beta = 1.257, 1.361, 1.466, 1.558$ corresponding to their investigated cases. This allows us to follow the experimentally realized bifurcations of tertiary states displayed in Figures 9, 6, 7 and 5 of HBA, respectively. It should be noted that a stability analysis has not been performed near the onset of the Taylor vortices, because those with a wavenumber smaller than the critical value are subject to the Eckhaus instability there, for which $d = 0$ and $|b| \ll 1$.

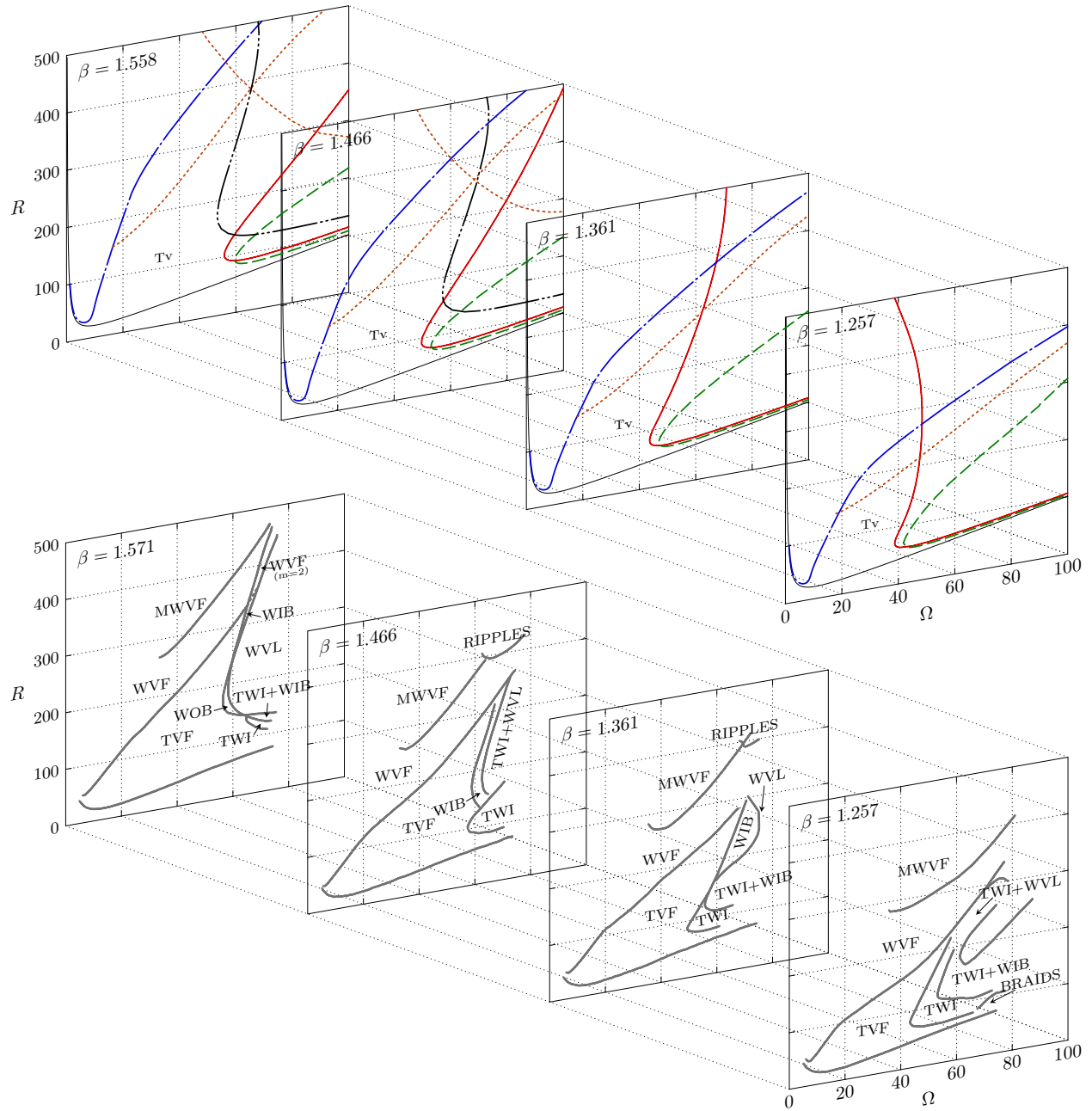


Figure 5: Instabilities of the Taylor vortex flow (Tv) leading to tertiary states for four values of β as indicated. In the upper part computed boundaries for the onset of the twist vortices (Twi, thick solid curves), wavy twists (Wtw, dashed curves), wavy vortex states (Wvf, dash-dotted curves), oscillatory wavy vortex states (Owv, dotted curves bifurcated at $\Omega \sim 20$), drifting wavy vortex states (Dwv, dotted curves decreasing with increasing Ω), subharmonic oscillatory wavy vortex states (Sow, dash-doubly-dotted curves) are shown for various values of β . The neutral boundaries for the various values of β are depicted with thin solid curves. The 3-dimensional projection of the theoretical results shows the effect of β on the stability boundaries. The experimental results of HBA are shown in the bottom part of the figures, which, in contrast to the theoretical results, include the onset of quaternary patterns.

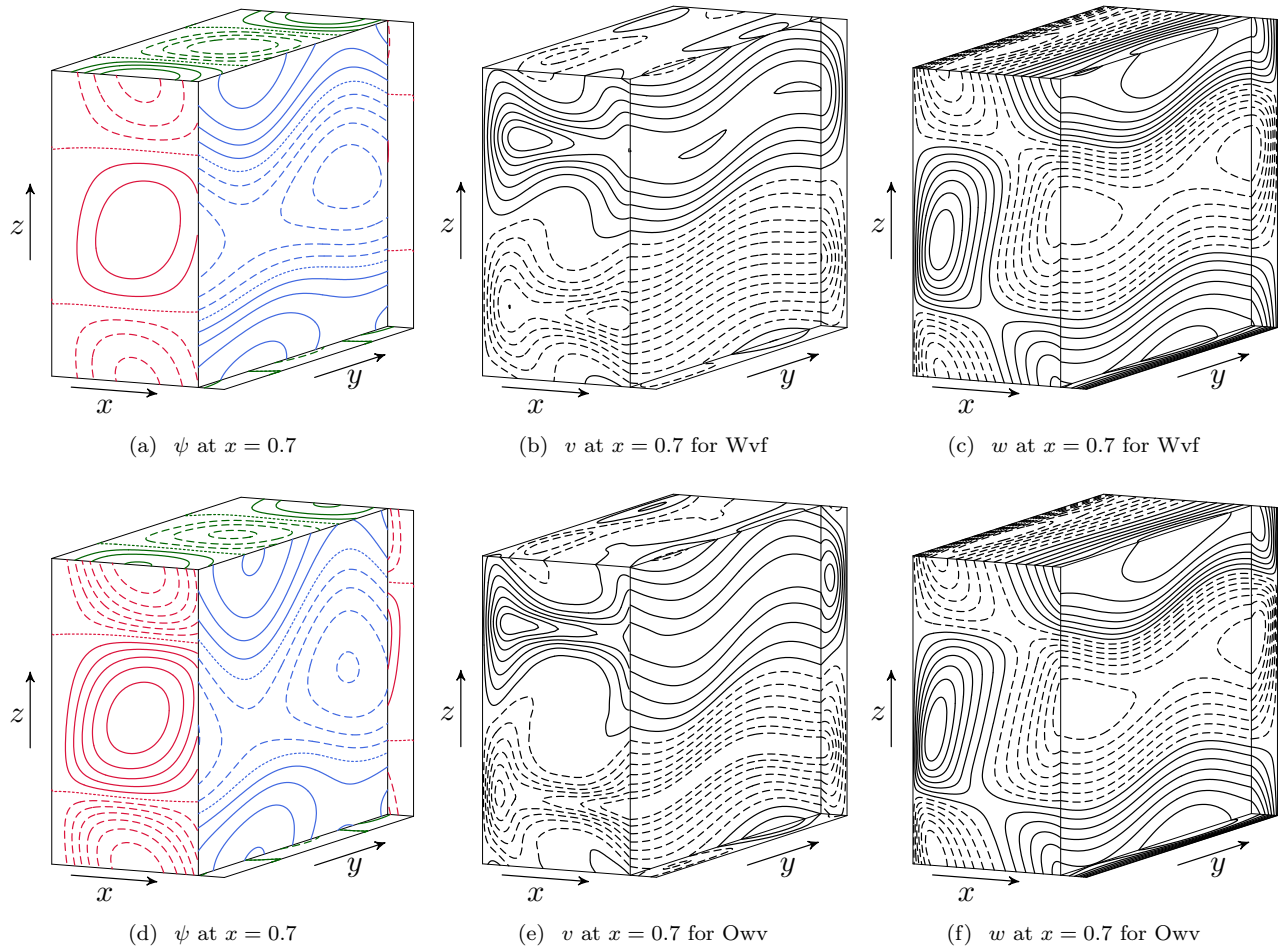


Figure 6: Tertiary states for $\beta = 1.25$, Wvf (upper row) and Owv (lower row), are visualised by the potential ψ in (a) and (d) for $(R, \Omega, \alpha) = (110, 15, 0.38)$ and $(180, 35, 0.27)$ respectively. ψ is plotted on the plane $x = 0.7$ in (a) and (d), whereas (b)-(c) and (e)-(f) are contour plots at $x = 0.7$ for the azimuthal, $v = \frac{\partial^2 \phi}{\partial x \partial y} + \frac{\partial \psi}{\partial z}$, and axial, $w = \frac{\partial^2 \phi}{\partial x \partial z} - \frac{\partial \psi}{\partial y}$, components of the velocity field for the tertiary states Wvf and Owv as indicated.

111 We start the presentation of our results with Figure 4 in which the stability boundaries of the axisymmetric Taylor
 112 vortex (Tv) for $\beta = 1.257$ are shown. Thus a direct comparison with Figure 9 of HBA can be performed. Predominant
 113 among the tertiary flows are the twist vortices (ordinary twists), as shown in Figure 5. The predictions of WBN for the
 114 onset of Twi have been confirmed by the experimental observations of HBA. However, the onset of Wtw, that are predicted
 115 to precede the onset of Twi at the low- R -branch, were not observed, as mentioned above. An explanation of this puzzle
 116 can be found in the experimental boundary conditions. Both types of the twist vortices, Twi and Wtw, differ from Taylor
 117 vortices in that they exhibit a z -independent columnar component which assumes the form $\phi_c = f(x) \exp(i\alpha y)$ in the
 118 case of Twi and $\psi_c = g(x) \exp(i\alpha y)$ in the case of Wtw. The former does not exhibit a z -component of the velocity and
 119 satisfies a stress-free condition at any boundary $z = \text{const}$. The adjustment to an experimental no-slip boundary at some
 120 $z = \text{const}$. thus requires only a minor modification of the solution. The z -component of the velocity in the Wtw case,
 121 $-\frac{\partial}{\partial y} \psi_c$, remains finite at all values of z and thus exhibits a finite normal component at any boundary $z = \text{const}$. Since
 122 this property requires a significant modification of the solution, it is not surprising that the onset of the Wtw instability
 123 is damped in experiments. Of course this effect will diminish when experiments are carried out with hundreds of vortices
 124 in the z -direction, but in the case of HBA the number of vortex pairs did not exceed 16. A similar but more tentative
 125 explanation for the absence of the Wtw mode in the experiments of HBA has already been given by AnS.

126 The dotted, solid, dashed and dot-dashed curves are stability boundaries with $b = 0$ and $d > 0$ (see equations (20)),
 127 whereas the dash-doubly-dotted curve is characterised by $b = \beta/2$ and $d \sim 0.6$. The boundary for the Eckhaus instability is
 128 not depicted because of its close proximity to the neutral curve, $R = \Omega + 113.5/\Omega$ in Figure 4, and the difficulty involved
 129 in its experimental detection. The solid, dashed, dot-dashed and dotted curves constitute the bifurcation curves of the
 130 tertiary states Twi, Wtw, Wvf and Owv, respectively. The right plot of the figure denotes the value of d , for which the
 131 maximum real part of sigma reaches a positive value.

132 As can be seen from Figure 4, there is a jump in the value of the parameter d , that exists between the Twi and Wtw
 133 stability boundary curves in the region defined by $(R, d) \sim (60, 1.2)$. All curves except for the dash-doubly-dotted curve (for

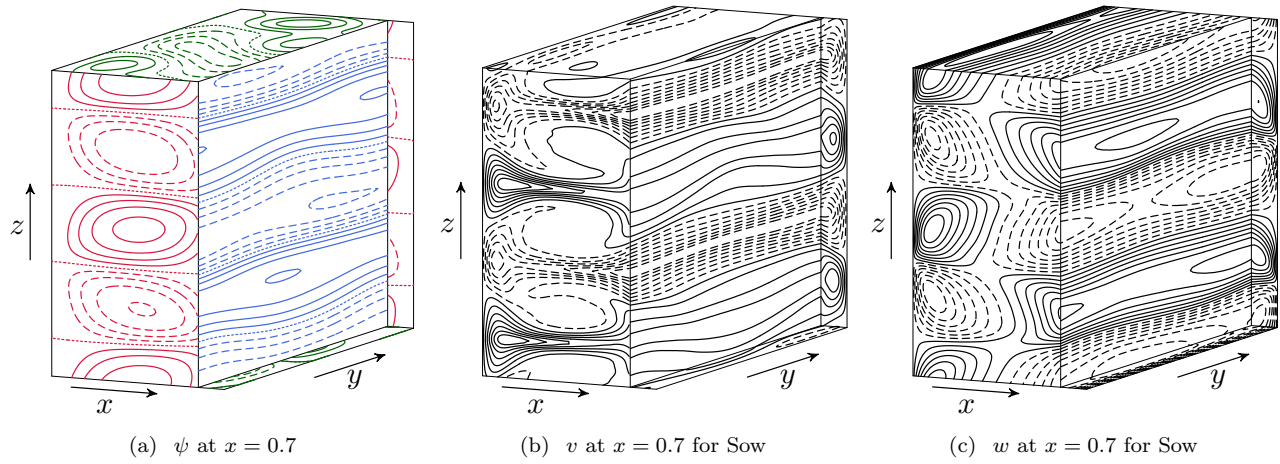


Figure 7: The tertiary subharmonic oscillatory wavy vortex state (Sow) is visualised by the potential ψ on the plane $x = 0.7$, whereas (b)-(c) are contour plots at $x = 0.7$ for the azimuthal, $v = \frac{\partial^2 \phi}{\partial x \partial y} + \frac{\partial \psi}{\partial z}$, and axial, $w = \frac{\partial^2 \phi}{\partial x \partial z} - \frac{\partial \psi}{\partial y}$, components of the velocity field for the tertiary state Sow. Here $(R, \Omega) = (200, 60)$ and $(\alpha, \beta) = (0.612, 0.733)$ corresponding to the Sow boundary depicted in the plot for $\beta = 1.466$ of Figure 5.

Sow) correspond to monotonic type instabilities. The dotted curve denotes the bifurcation curve of the tertiary oscillatory wave vortex (Owv). We show contour plots of the tertiary Wvf and Owv states in Figure 6. The tertiary Wvf is a steady state solution, while the tertiary Owv represents a standing oscillation with frequency $\omega \approx 20$ at $(R, \Omega) \approx (160, 20)$. Both states, Wvf and Owv, do not have a mean flow component in the axial direction. Additionally the Wvf and Owv states have the same symmetry and their main difference is that Owv possesses oscillating coefficients. They hardly differ in the shape of their vector potential as is evident from Figure 6. In the experimental situation it is difficult to distinguish the Wvf and Owv states since both are propagating relative to the laboratory frame of reference. For this reason the observations of HBA show only a single stability boundary denoted by Wvf in Figure 5 in place of the dash-dotted and dotted curves of the theoretical results.

In Figure 5 the stability boundaries for the four β values are shown which correspond to the β -values that are depicted in Figures 5, 6, 7 and 9 of the experimental study of HBA. For a direct comparison between theory and experiment, we have redrawn the HBA experimental results, including their preferred nomenclature, in the same Figure 5. While the stability boundary for the onset of the ordinary twist vortices (Twi) agrees reasonably well with the observations as noted by HBA, there is no indication for the onset of the wavy twist vortices (Wtw) found in the experimental observations, for the reason explained above. In the comparison between theory and experimental observations it should be kept in mind that the similarities of the shapes of the stability boundaries is of primary importance. A shift in the (R, Ω) -plane can easily be explained by the difference in the radius ratio r_i/r_o . In all figures the solid curve corresponds to the onset of Twi, the long-dashed curve to the onset of Wtw, the short-dashed curve to the onset of Oscillatory wavy vortex flow (Owv) and the dash-dotted curve to the onset of the Wavy vortex flow (Wvf). It is quite obvious from Figure 5 that the stability boundaries vary considerably with the basic span-wise wavenumber β .

In fact, as the value of β increases beyond about 1.4 the onset of the tertiary subharmonic oscillatory wavy vortex (Sow) appears and replaces the onset of Twi. The corresponding stability boundary of Taylor vortices, named SUBL in NAG, is nearly independent of Ω . The bifurcating solution Sow is depicted in Figure 7. Near onset the Sow states are weakly oscillating. Further away from onset the oscillations increase in amplitude. For the case $\beta = 1.558$ the Sow state is a standing oscillation with $\omega \approx 65$ for $(R, \Omega) \approx (140, 55)$.

4.2. Quaternary states

A large amount of information on flows beyond the tertiary states in the Taylor-Couette system has become available through the work of HBA. Although the ratio between inner and outer radius of the rotating co-axial cylinders differs significantly from unity in the experiments of HBA, the agreement between theoretical predictions and experimental observations for the transitions to quaternary states is still quite good, as we show in Figure 8. Here we have superimposed the actual experimental observations (dashed curves with squares) for comparison. The value of the axial wave number of the Twi is $\beta = 1.25$. The onset of the quaternary states, according to our computations, is indicated by the thick solid-dash and solid-doubly-dashed curves for the states Sowv and Swib/Swob respectively.

According to HBA the Swib and Swob are characterised by azimuthally traveling waves, which are most apparent near the inflow boundaries or the outflow boundaries of the vortices. According to our simulations the quaternary states Swib and Swob have the following characteristics: they are subharmonic states that have bifurcated from the Twi with a 3×2 subharmonicity, i.e. three vortices in the azimuthal direction and two vortices axial direction are present, as shown in

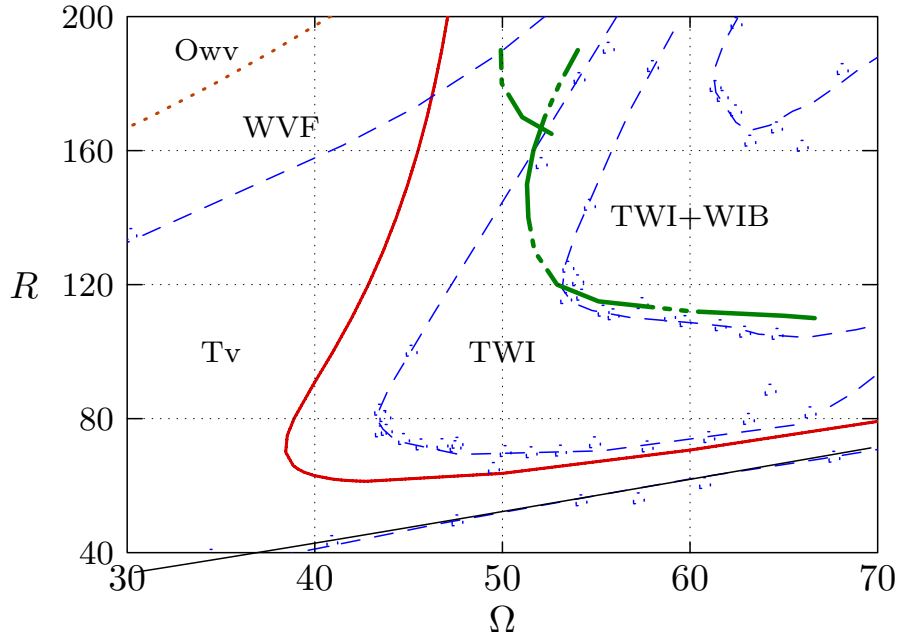


Figure 8: Stability boundaries are indicated by the thick solid-dashed and solid-doubly-dashed curves for the onset of the quaternary states Sowv and Swib/Swob, respectively. These curves were determined by the values of $(d, b) = (\alpha/2, \beta)$ and $(\alpha/3, \beta/2)$, for which the most unstable disturbances appear. Herein $\alpha \sim 1.8$ and $\beta = 1.25$. The stability boundaries of the Twi and Owv are depicted by the solid and dotted curves, respectively. We have also indicated by dashed curves and little squares the stability boundaries observed in the HBA experiment for $\beta = 1.257$. WVF, TWI and TWI+WIB refer to the experimental results in Figure 9 of HBA.

ℓ	Poloidal	Toroidal	V
odd	$\phi_{\ell mn}^{\text{Swib}} = (\phi_{\ell mn}^{\text{Swob}})^*$	$\psi_{\ell mn}^{\text{Swib}} = -(\psi_{\ell mn}^{\text{Swob}})^*$	$V_{\ell}^{\text{Swib}} = V_{\ell}^{\text{Swob}}$
even	$\phi_{\ell mn}^{\text{Swib}} = -(\phi_{\ell mn}^{\text{Swob}})^*$	$\psi_{\ell mn}^{\text{Swib}} = (\psi_{\ell mn}^{\text{Swob}})^*$	$V_{\ell}^{\text{Swib}} = -V_{\ell}^{\text{Swob}}$

Table 4: An example set of coefficients for the symmetry of the Swib/Swob states. Here superscript * denotes the complex conjugate. Neither Swib nor Swob state has a W component of the mean flow.

Figure 9. The quaternary states Swib/Swob bifurcate in pairs and they drift in the azimuthal y -direction with opposite phase speed $|c| \approx 70$ at $(R, \Omega) \approx (120, 53)$. They are characterised by the following symmetry properties:

$$\text{Swib}(t, x - x_0, y - y_0, z - z_0) = \text{Swob}(t, x_0 - x, y_0 - y, z_0 - z).$$

In Table 4 we present the properties of the coefficients of Swob/Swib for the poloidal, toroidal and mean flow in the azimuthal and axial directions. Because of this mirror symmetry the plots of Swib in figure 9 are converted into the plots of Swob when (x, y) is converted into $(-x, -y)$ and z is replaced by $z + \pi/\beta_0$. We note that as the Swob/Swib solutions are followed away from their points of bifurcation their coefficients become increasingly oscillatory.

The quaternary Sowv solution is a subharmonic solution (a double vortex structure in the azimuthal direction) and exhibits a standing oscillation with $\omega \approx 45$ for $(R, \Omega) \approx (165, 53)$, with a Wtw type of symmetry as shown in Figure 10.

5. Concluding remarks

From a superficial point of view the result of the paper should compare well with the experimental results presented by TTA and SSA. But the latter are strongly affected by the end effects in the y -direction of the experiment and by the restriction to relatively low rotation rates. On the other hand we have found rather good agreement with the cylindrical experiment of HBA. The primary goal of our analysis has not been the optimisation of the comparison between theory and experiment. Rather the goal has been to contribute to the understanding of the bifurcation structure of one of the most basic systems of fluid dynamics. As we have shown not all features of the idealised system such as the transition to Wtw may be realised in the experiment because of the restricted axial direction of the apparatus. Nevertheless the planar limit of the Taylor-Couette system with its high symmetry will always be a relevant state of reference.

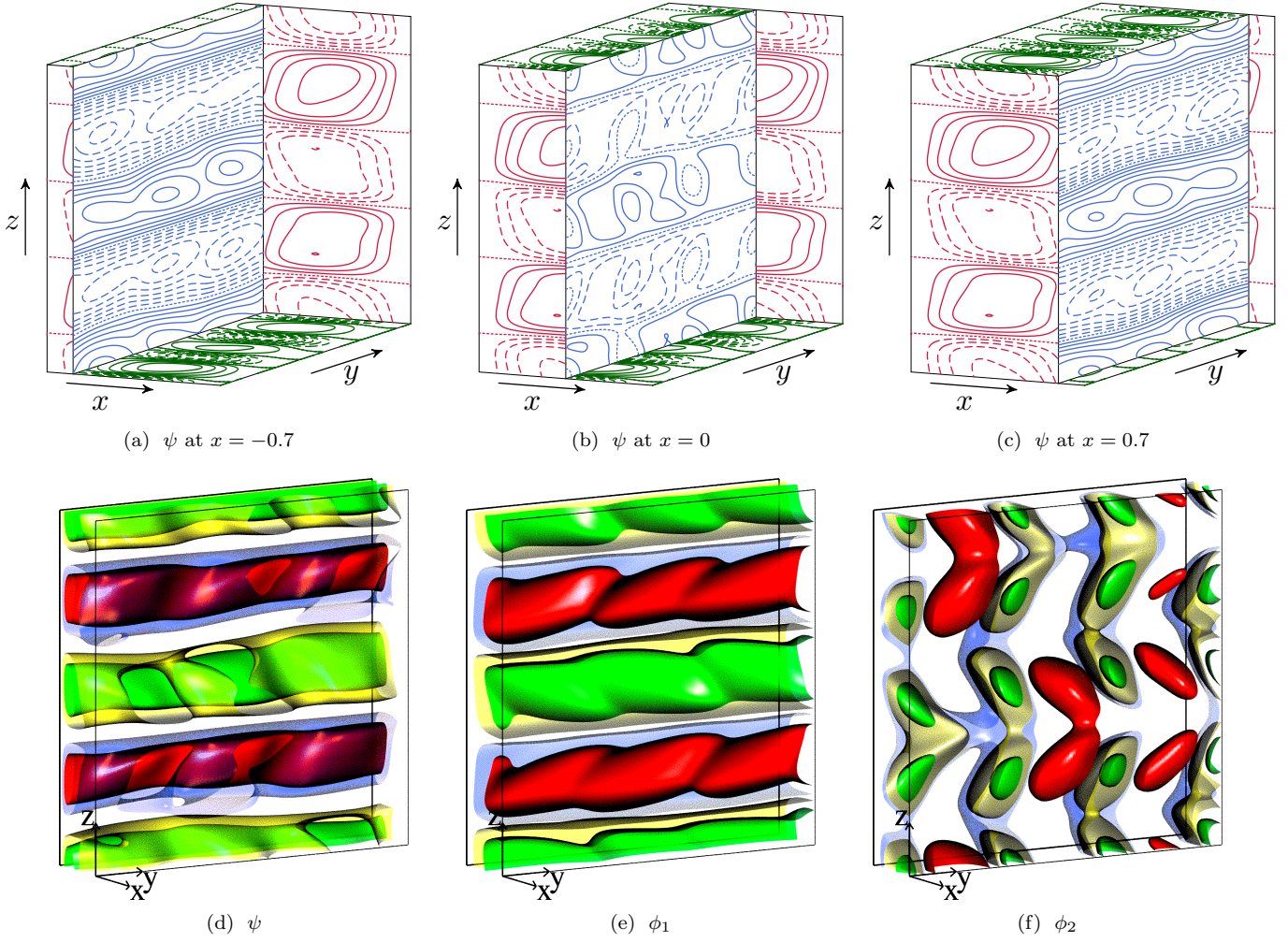


Figure 9: The quaternary state Swib for $(R, \Omega) = (130, 53)$ and $(\alpha, \beta) = (\beta_0/3, \beta_0/2)$ visualised by the vector potential (ψ, ϕ_1, ϕ_2) , where $\beta_0 = 1.25$. ψ is plotted on the planes (a) $x = -0.7$, (b) $x = 0$, and (c) $x = 0.7$, whereas ϕ_1 and ϕ_2 are plotted on the planes perpendicular to the unit vectors \mathbf{j} and \mathbf{k} , respectively. Note that the quaternary state Swib is the result of the subharmonic instability of the Twi with the multiple factors three and two in the azimuthal and axial directions. The displays (d-f) show the stream functions ψ , ϕ_1 and ϕ_2 visualized at the iso-surfaces 0.02 (dark green), 0.25 (pale yellow, 0.35 for ϕ_1 and 0.4 for ϕ_2), 0.75 (very pale blue, 0.65 for ϕ_1 and 0.5 for ϕ_2) and 0.98 (very dark red) in a periodic box with $x \leq 0$, where the ranges of $|\psi|/R \leq 0.340$, $|\phi_1|/R \leq 0.111$ and $-0.031 \leq \phi_2/R \leq 0.019$ have been mapped onto $[0,1]$. The figure also applies for Swob, when x and y are replaced by $-x$ and $-y$ and when z is replaced by $z + \pi/\beta_0$.

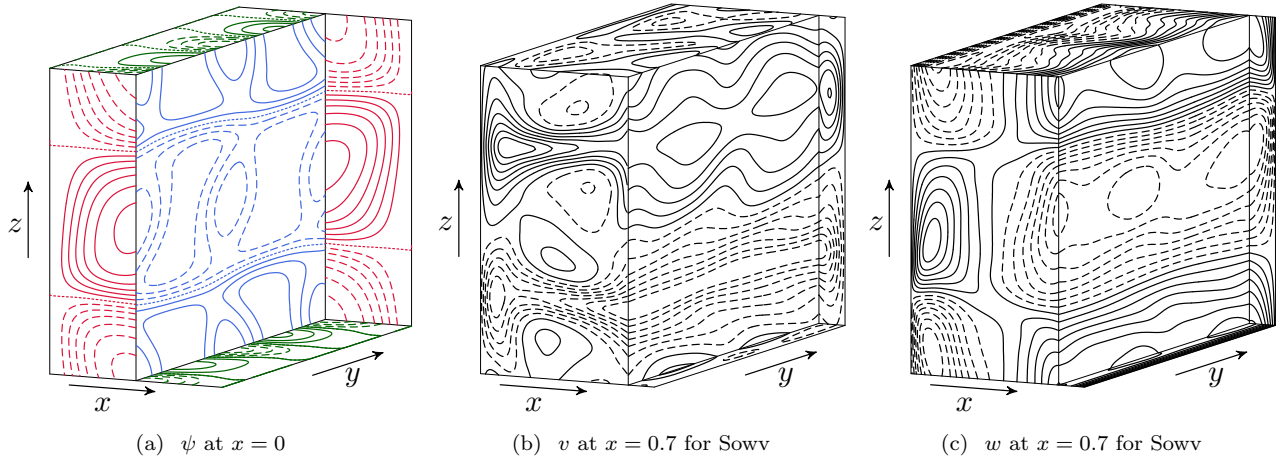


Figure 10: The quaternary state Sowv for $(R, \Omega) = (180, 52)$ and $(\alpha, \beta) = (0.9, 1.25)$, that bifurcates from the azimuthally subharmonic vortices of Twi, is shown by the potential ψ . ψ is plotted on the plane (a) $x = 0$, whereas (b)-(c) are contour plots at $x = 0.7$ for the azimuthal, $v = \frac{\partial^2 \phi}{\partial x \partial y} + \frac{\partial \psi}{\partial z}$, and axial, $w = \frac{\partial^2 \phi}{\partial x \partial z} - \frac{\partial \psi}{\partial y}$, components of the velocity field for the quaternary state Sowv.

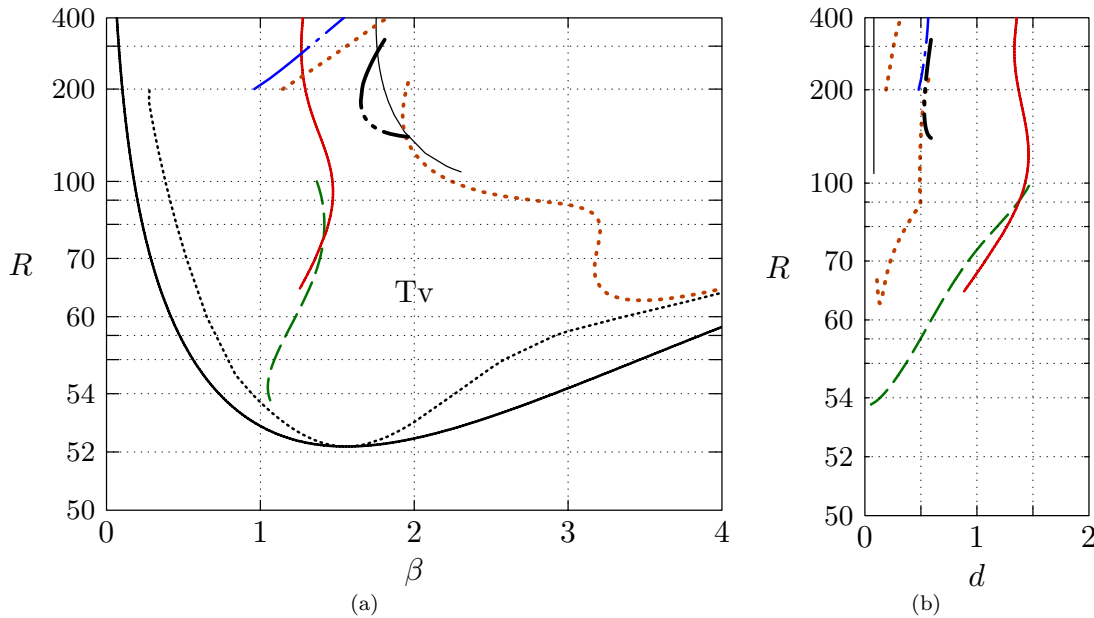


Figure 11: Linear stability of Taylor vortex flow for $\Omega = 50$ and $(L, M, N) = (25, 0, 25)$. Onsets of the ordinary twists (red solid curve), wavy twists (green dashed curve), nearly columnar (orange dotted curve at lower R), Owv (orange dotted curve at higher R), Wvf (blue dash-dotted curve) and a subharmonic oscillatory state (black dashed-doubly dotted curve) are shown. The thin solid curve indicates an instability with $(d, b) = (0.1, 0)$. The values of d for which the maximum of σ_r reaches zero are shown in the plot on the right side. The Eckhaus instability, close to and above the neutral curve, is indicated by the narrow dotted curve in black.

182 In order to show the dependence of the stability boundaries on β from a different point of view, we have plotted in
 183 Figure 11 stability boundaries of Taylor vortex flow in a R versus β plot for a fixed $\Omega = 50$. In this figure the onsets of
 184 the ordinary twists (red solid curve), wavy twists (green dashed curve), nearly columnar states (blue dash-dotted curve),
 185 and subharmonic oscillatory states (black dashed-two dotted line) are shown. The values of d for which the maximum
 186 of σ_r reaches zero are indicated in the plot on the right side and the curves between the two plots are in one to one
 187 correspondence. Here we have also plotted the Eckhaus instability, which shows its proximity to the neutral curve. We
 188 note that the Twi and Wtw onset curves cross at $(R, \beta) \sim (75, 1.35)$.

189 As is indicated in Figure 11 for higher values of beta up to $\beta \sim 3$ rather narrow Taylor vortices may be realized for
 190 $R < 80$. These vortices will become unstable to states with columnar components with increasing R . Around the minimum
 191 of the orange-dotted curve, and in particular for low R , $(R, \beta) \sim (62.2, 3.5)$, a state with a strong columnar component
 192 drifting in stream-wise direction has been found for $d \sim 0.17, \beta = 3.5$ (see Figure 11). No corresponding experimental
 193 observations have been found in the literature. We hope that this discovery will stimulate experimenters to investigate
 194 this interesting part of the parameter space.

195 6. Acknowledgments

196 This work was supported in part by a Marie Curie IIF (Grant no. 298891) from the European Union and by the
 197 Leverhulme Trust (Grant no. VP1-2012-017).

198 7. References

- 199 [1] C. D. Andereck, S. S. Liu, H. L. Swinney, Flow regimes in a circular Couette system with independently rotating
 200 cylinders., *J. Fluid Mech.* 164 (1986) 155–183.
- 201 [2] L. S. Tuckerman, Taylor vortices versus Taylor columns., *J. Fluid Mech.* 750 (2014) 1–4.
- 202 [3] R. Tagg, The Couette-Taylor problem, *Nonlinear Sci. Today* 4 (1994) 2–25.
- 203 [4] E. Weisshaar, F. H. Busse, M. Nagata, Twist vortices and their instabilities in the Taylor-Couette system., *J. Fluid*
 204 *Mech.* 226 (1991) 549–564.
- 205 [5] J. J. Hegseth, G. W. Baxter, C. D. Andereck, Bifurcations from Taylor vortices between corotating concentric
 206 cylinders., *Phys. Rev. E* 53 (1996) 507–521.

- 207 [6] T. Tsukahara, N. Tillmark, P. H. Alfredsson, Flow regimes in a plane Couette flow with system rotation., *J. Fluid*
208 *Mech.* 648 (2010) 5–33.
- 209 [7] A. Suryadi, A. Segalini, P. H. Alfredsson, Zero absolute vorticity: Insight from experiments in rotating laminar plane
210 Couette flow., *Phys. Rev. E* 89 (2014) 033003.
- 211 [8] M. Nagata, Tertiary solutions and their stability in rotating Plane Couette flow, *J. Fluid Mech.* 358 (1998) 357–378.
- 212 [9] C. A. Daly, T. M. Schneider, P. Schlatter, N. Peake, Secondary stability and tertiary states in rotating plane Couette
213 flow, *J. Fluid Mech.* 761 (2014) 27–61.
- 214 [10] N. Tillmark, P. H. Alfredsson, Experiments on rotating plane Couette flow, in: L. M. S. Gavrillakis, P. A. Monkewitz
215 (Eds.), *Advances in Turbulence VI*, Kluwer, 1996, p. 391.
- 216 [11] J. Antonijoan, J. Sánchez, Transitions from Taylor vortex flow in a co-rotating Taylor-Couette system, *Physics of*
217 *Fluids* 12 (2000) 3147–3159. doi:10.1063/1.1313385.
- 218 [12] S. Chandrasekhar, *Hydrodynamic and hydromagnetic stability.*, Oxford University press (1961) 272.
- 219 [13] M. Nagata, On wavy instabilities of the Taylor-vortex flow between corotating cylinders, *J. Fluid Mech.* 188 (1988)
220 585–598.